Pergamon

Cement and Concrete Research, Vol. 28, No. 1, pp. 103–114, 1998

0008-8846/98 $19.00 + .00

PII S0008-8846(97)00221-4

CRACK GROWTH MECHANISMS IN FOUR DIFFERENT CONCRETES: MICROSCOPIC OBSERVATIONS AND FRACTAL ANALYSIS

B. Chiaia,[1] J.G.M. van Mier,[2] and A. Vervuurt
Faculty of Civil Engineering, Delft University of Technology, GA 2600 Delft, The Netherlands

(Received May 23, 1997; in final form October 20, 1997)

ABSTRACT

Splitting tests have been carried out for evaluating damage in four types of concrete. The concretes contained either river gravel with maximum aggregate size equal to 2 and 16 mm, phosphorous-slag aggregates, and Lytag aggregates. Different failure behaviours have been revealed, mainly depending on the aggregate and interface characteristics. The microscopic cracking mechanisms strongly affect strength, toughness, and ductility. In addition to mechanical measurements, a high resolution optical microscope was adopted for detecting the crack growth. Fractal dimensions of the crack lips and of the complex damage patterns were computed. No simple relation exists between fracture energy and fractal dimension, but relative differences in the material structure affect the value of the fractal dimension. This confirmed the peculiar different behaviours encountered in the tests. © *1998 Elsevier Science Ltd*

Introduction

In heterogeneous materials such as concrete, sandstone, and rock, the weakest link is generally represented by the interfacial zone between two dissimilar materials. For normal weight concrete specifically, the bond zone between (mortar or cement) matrix and aggregate particles is considered to be the weakest element in the material structure (1). However, it seems that not only does the strength of the interface play a dominant role in crack initiation, but more meaningfully, the combination of stress and strength also. In fact, the material is most likely to fail at the point with the highest stress relative to its strength. At the interface between matrix and aggregate, the two dissimilar materials meet but retain their considerably different identities in Young's moduli. This results in stress concentrations. Combined with the relatively low strength, this zone becomes of major importance for crack initiation and propagation. After an entropic stage of diffused microcrack nucleation at interfaces, these zones, together with pre-existing microdefects, become "attractors" for the subsequent macrocrack development. The overall material response is highly dependent on the distri-

[1]Permanent Affiliation: Department of Structural Engineering, Politecnico di Torino, Corso Duca degli Abruzzi 24, Torino, Italy.
[2]To whom correspondence should be addressed.

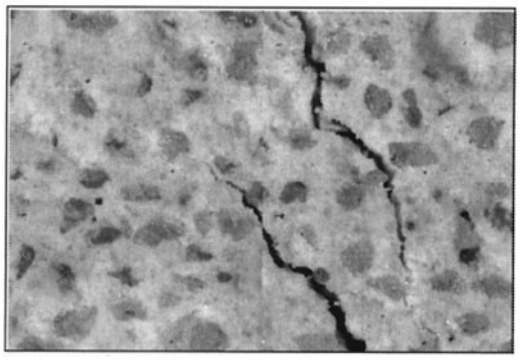

FIG. 1.
Bridging in the matrix of the phosphorous-slag concrete.

bution of these attractors and on their tendency to connect and coalesce. The process from microcracking to macrocracking is thus characterized by interfacial cracks growing through the matrix and joining into macrocracks. The macrocracks remain discontinuous during a very long time. In the softening stage, the crack faces are still connected by the so-called crack face bridges (2). These bridges (Fig. 1) provide for stress transfer, and explain the long stable tail of the tensile softening curve.

In the Fictitious Crack Model (3), a cloud of microcracks ahead of the macroscopic crack tip is assumed. For concrete, however, the method seems mainly based on requirements for analytical treatment of the material behaviour rather than on a physical mechanism, as was shown in previous experiments (2). In order to apply this model, the fracture energy should be a constant value, regardless of the size of the specimen or the specific boundary conditions. The question remains, however, whether this is true, because normally it is assumed that the work of fracture can easily be determined from the area under the stress-crack opening response of a uniaxial tensile test. In such a test, the fracture energy G_F is determined by dividing the total work of fracture W_F by the net area A of the specimen cross-section ($G_F = W_F/A$). From experiments, however, a strong size effect is observed (4), indicating that additional energy dissipation occurs outside the localization zone. Physically, the dependence of GF on the specimen's size can be adequately explained by considering energy dissipation to occur in an invasive fractal domain with Hausdorff dimension larger than 2.0 (4). Energy flow is thus intermediate between surfacial and volumetric dissipation.

In this paper we will not further discuss the effects of size on fracture energy and strength, but rather emphasize the microscopic fracture mechanisms in concretes containing different types of aggregates. When various materials are used in a concrete composite, different microscopic failure mechanisms are observed at the interface between matrix and aggregate particles. Because the fracture process is a hierarchical multiscale phenomenon, different basic micromechanisms imply different macroscopic failure modes. It will be shown that bridging represents a major toughening mechanism, which comes into play at different scales, depending on the microstructure. It was already shown (2) that the crack face bridges in lightweight concrete ($d_{max} = 12$ mm for Lytag) loaded in uniaxial tension are of comparable size to bridges observed in a mortar with $d_{max} = 2$ mm.

In the present study, four types of concrete have been subjected to indirect tensile loading. The setup was developed at the Stevin Laboratory of Delft University of Technology, and

comprises a completely new loading device in which a perfectly horizontal splitting load can be applied to concrete specimens (5). The concretes contained either river gravel with maximum aggregate size equal to 2 and 16 mm, phosphorous-slag aggregates, or Lytag aggregates. The damage evolution during the fracture process has been monitored with a long-distance optical microscope, thus permitting us to view the peculiar micromechanisms of failure in each material.

Fractal analysis of the damage patterns and of the crack lips has been carried out for all the mixtures. Image processing algorithms have been developed to extract the crack topology from the digitized images. The box-counting method has been applied to the filtered images, in which the fractal characteristics have been highlighted. It is shown that the fractal analysis can successfully describe the progressive vanishing of microstructural disorder effects, which is related to different scales of observation of the fracture process. Moreover, fractality comes into play also at the level of the single aggregate, as in the case of the through-particle cracks occurring in the Lytag composite. No clear correlation can be deduced between the fractal dimensions and the fracture energy values for the different concretes, but relative differences in the material structure affect the value of the fractal dimension. It can be confirmed that the most relevant effect of fractality is represented by the crack-resistance behaviour encountered in the tests (6).

Loading Equipment and Material Characteristics

In this section, the specimen geometry, the material characteristics and the experimental set up will be described. Owing to the limitations of the optical device, (the microscope monitors only the surface of the specimen), relatively thin specimens were used. Another reason for the thinness of the specimens was that the aim of the experiments is to validate a two-dimensional numerical model (7,8).

The specimens, with planar dimensions of 125 $\times$ 170 mm (Fig. 2a), had a constant thickness of 15 mm. To fix the position of crack initiation, a 30-mm-deep notch was sawn at half the width of the specimen. An open frame has been developed, in which the specimen was positioned during testing. At the top of the specimen, two loading platens were glued, between which a perfectly horizontal splitting load could be applied. The specimen was supported at the bottom with a small strip of steel (15 mm width), because the high-resolution long-distance microscope requires a fixed position of the specimen for studying the concrete surface. Next to the strip and the two supports to which the load is applied, three spring supports were also attached at the back of the specimen, to ensure co-planarity of the specimen surface and of the microscope during the entire loading sequence.

A completely new device was developed for applying the load upon the specimen (Figs. 2b, c). To avoid vertical stresses in the specimen during loading, a horizontal splitting load was applied, rather than the more common wedge splitting load (9). In the latter tests, which can be carried out in a standard compression machine, strong frictional effects caused by the wedge may significantly affect the results, especially in the tail of the softening curve. The load was applied through a symmetric hydraulic actuator, consisting of a single oil reservoir and two pistons, one at each side of the central reservoir. The load was measured using two miniature Sensotec load cells (type LFH-7I/280–01), which can measure a maximum load of 1 kN (250 lbs) each. The experiments were carried out under displacement control, in which the average crack mouth opening displacement (CMOD) was used as the feedback signal for

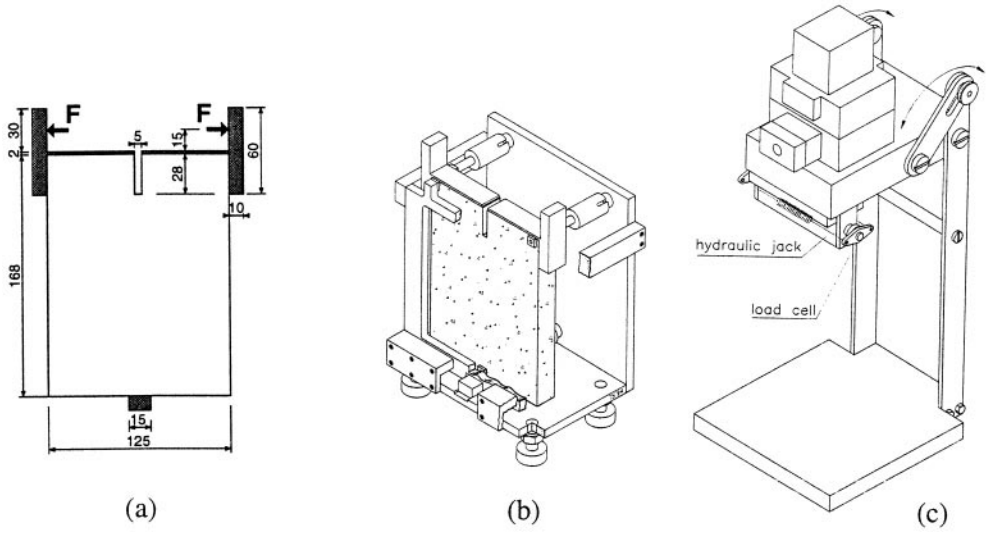

FIG. 2.
Specimen geometry (*a*) and schematic view of the test assembly (*b*, *c*).

the closed loop servo-controlled system. For the displacement measurements, two LVDTs with a measuring length of 15 mm were glued across the top of the notch, at each side of the specimen. The CMOD was calculated as the average of these two LVDTs and was monitored either until complete fracture of the specimen occurred, or up to a maximum CMOD approximately equal to 160 mm. In this way it was possible to measure not only the maximum load P_u but the total work of fracture (W_F) as well. From W_F, the specific energy dissipation per unit area can be calculated. It should be mentioned that these values of G_F have to be interpreted as nominal values, because they are computed by dividing the work of fracture by a nominal fracture area A_{nom} resulting from the (macroscopic) length of the final main crack. For this purpose, the crack length was measured after complete failure of the specimen.

Four different types of concrete were investigated. For maximum contrast in the microscope images, a white Portland cement (Blanc BEL P40) was used. For the first two mixtures, specimens were cast using traditional river gravel with maximum size of 16 mm (Con16) or 2 mm (Con2). Because of increasing interest in environmental issues, industrial rest-products are used more frequently nowadays for the fabrication of aggregate particles for concrete. A mixture was made containing phosphorous-slag aggregates (ConPS). Phosphorous slag is the dross separated in a fused state during the extraction of phosphor from natural minerals. The slag closely resembles some volcanic scoria, and its vitreous consistency accounts for its hardness and strength. In contrast to this very dense type of aggregate, an extremely porous and lightweight aggregate (Lytag) was also used. Such aggregates can be very useful when the dead weight of a structure has to be minimized. Lytag is produced by sintering pulverized fly-ash (released as a rest-product in coal-burning energy power plants) mixed with powder coal particles. The Lytag aggregate particles were placed in fresh tap water 1 day before casting, in order to completely saturate the highly porous material. Subsequently, the

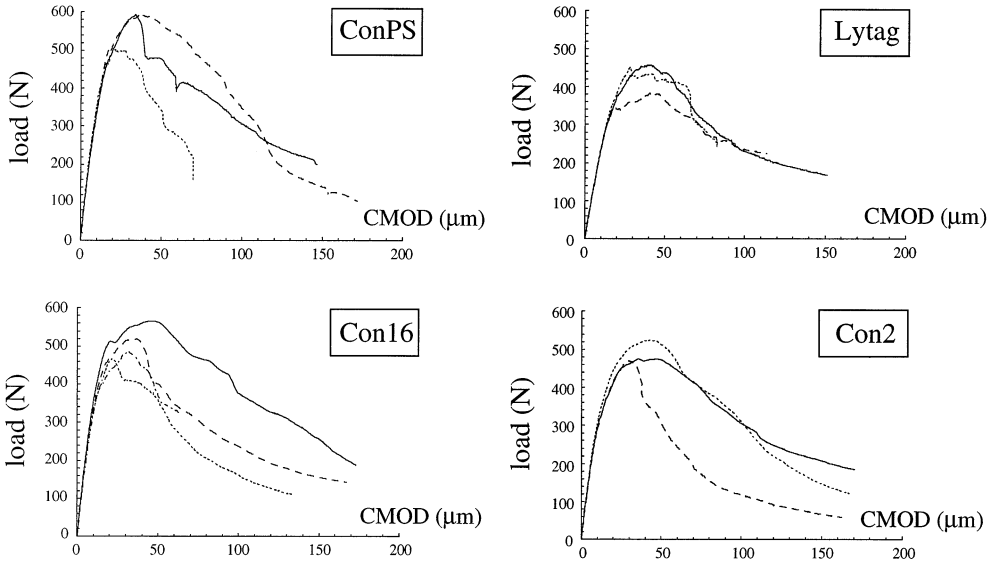

FIG. 3.
Experimental load-CMOD curves from splitting tests.

particles were surface-dried for about 24 h under lab conditions (note that the dry material can absorb up to 20% of water).

At least two different batches were prepared for each mixture. The four types of concrete were cast in moulds of 200 × 200 × 200 mm^3. One day after casting, the blocks were demoulded and placed under water. After 28 days of hardening, the specimens were sawn from the central part of the block and placed back under water until 1 h before testing. The age at testing varied between 29 and 32 days after casting. For reference, additional (load-controlled) standard compression and brazilian tests were carried out on 150-mm cubes. Very high strength values were obtained by ConPS, whereas the Lytag mixtures provided the lowest strength values (10).

Deformation-controlled splitting tests on the notched specimens were carried out, and the load-CMOD diagrams were monitored (Fig. 3). Because the maximum CMOD fluctuated widely among the specimens, a comparable evaluation of toughness was obtained by computing the work of fracture up to CMOD = 100 mm, which was reached in almost all the experiments (see Fig. 3). From this work of fracture, the nominal fracture energy G_F can be calculated. The phosphorous-slag concrete (ConPS) shows the highest peak load, whereas Con16 is characterized by the highest fracture energy. However, the G_F values are strongly dependent on the computed crack length. If the 100-mm work of fracture (W_F) is selected as a representative measure of toughness, it must be concluded that ConPS has the largest toughness. On the other hand, if the ratio between fracture energy and tensile strength is taken as a measure of ductility, phosphorous-slag concrete is the most brittle of the four mixtures, whereas Con16 is the most ductile material (see Table 1). Indeed, this can be expected if one observes the slopes of the softening branches, which are steeper in the case of the ConPS. In fact, this material is characterized by pronounced local instabilities, due to the high stiffness

TABLE 1
Measured fractal dimensions and mechanical properties of the four concretes.

Image →	High resol. (0.71 pix/μm)		Standard res. (0.278 pix/μm)		Mosaics high res.	
Concrete	min-max	mean	min-max	mean	min-max	mean
Con16	1.16–1.33	1.25	1.09–1.22	1.14	1.05–1.20	1.13
Con2	1.08–1.30	1.18	1.07–1.19	1.10	1.05–1.16	1.10
Lytag	1.13–1.35	1.24	1.05–1.20	1.10	1.04–1.15	1.09
ConPS	1.14–1.29	1.18	1.08–1.20	1.14	1.07–1.18	1.13

of the phosphorous aggregate, which leads to rather brittle interface cracking, as will be clarified in the next sections.

The relative brittleness of lightweight concrete is usually explained by the weakness of the Lytag particles, which causes a limited crack-arresting capacity. On the other hand, through-particle cracks may also propagate in a stable manner. As it will be shown in the following, Lytag particles can be considered strongly heterogeneous at the microscale. The fractal dimension of cracks through these particles can be quite high, when compared to the fractal dimension at the macrolevel of observation. This may be the reason for the relevant ductility (G_F/P_u) found in the Lytag concrete, which is not trivial when compared to its low nominal fracture energy and strength. It is interesting to note that the results of the Lytag and the Con2 are characterized by a much lower scatter in the mechanical properties, as compared to the Con16 and ConPS. In the case of the Lytag, quite remarkably, the three load-CMOD curves almost overlap. This can be explained by the lower degree of microstructural disorder at the specimen level. The lightweight concrete is characterized by uniform mechanical properties for both the matrix and the particles. The Con2 is a finer-grained mixture. As will be explained further on, a more rapidly vanishing fractality occurs in these materials, accompanied by less pronounced scale effects.

Optical Data Acquisition and Image Processing

In order to retrieve more detailed information regarding the (micro) cracks that develop at the surface of the specimen, real-time measurements were performed with a high-resolution long-distance optical microscope. A QUESTAR Remote Measurement System was used. The system was already available, and proved to be very useful for explaining failure mechanisms in concrete (2). In those early tests the system was suitable for manual scanning only. Recently (5), however, the system has been adapted for digitizing images and automatically storing and rescanning the crack path. The path along which images are taken is adjusted as cracking proceeds.

The microscopy system consists of a QUESTAR microscope (QM100 MK-III), which is connected to an Ikegami (ICD-46E) black and white CCD Camera for retrieving the images. Through a variable-scan framegrabber (VP-1400-KIT-768-E-AT) the images are digitized and stored in binary format in the hard disk of a personal computer. The microscope and the camera are fixed on a cradle that can be moved with stepper motors (Compumotor A/AX57–

TABLE 1
Continued.

Mosaics standard res.		G_F	ductility G_F/P_u
min-max	mean	N/m	$m \cdot 10^{-3}$
1.06–1.13	1.08	36.1	1.21
1.02–1.04	1.03	27.8	1.12
1.03–1.08	1.04	22.1	0.87
1.05–1.14	1.07	30.9	0.84

51) in three orthogonal directions. The stepper motors are controlled through a four-axis indexer (Compumotor AT6400) from the same PC where the images are recovered. The accuracy of the stepper motors is approximately 1 mm and the range is about 50 mm. The microscope operates at a distance of 200–225 mm from the specimen surface, depending on the selected magnification factor. During the test, the specimen is illuminated by two optic fiber arms connected to a AIMS FB-150 light source.

The images passed by the camera have a size of 756 × 512 pixels, each pixel representing a gray level between 0 (black) and 255 (white). For scanning the specimen with the microscope, an imaginary grid is projected on top of the specimen, each cell in the grid representing a single image. A small overlap of the images is taken into account in the selected cell size. The microscope provides five magnification factors, of which only two are used because too-large magnification factors would cause focusing problems due to the roughness of the specimen surface. In these experiments, the largest magnification factor provides a resolution of 0.71 pixel/mm^2, whereas the smallest factor (0.28 pixel/mm^2) is used for retrieving wider damage zones. Another method for retrieving more global crack information is scaling several high-resolution images to a 756 × 512 format and pasting them together in a mosaic of the completely scanned crack pattern (Fig. 4). The reduction factor depends of course on the number of images used in the mosaic. For computing the fractal

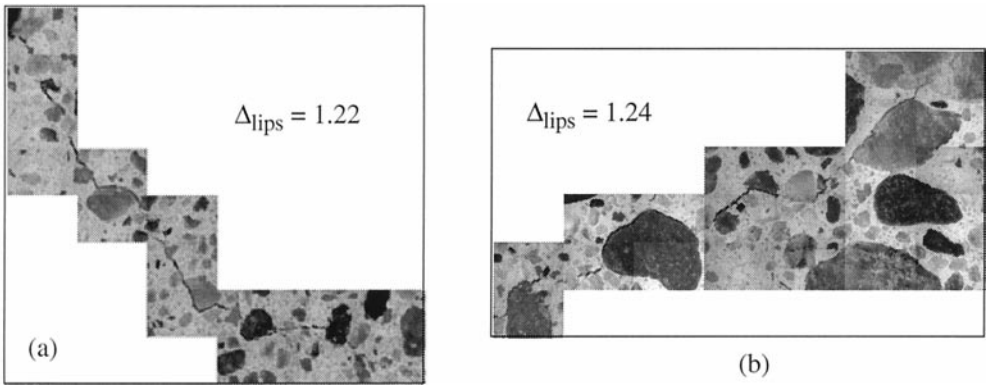

FIG. 4.
Crack path mosaic from Con2 (*a*) and from Con16 (*b*).

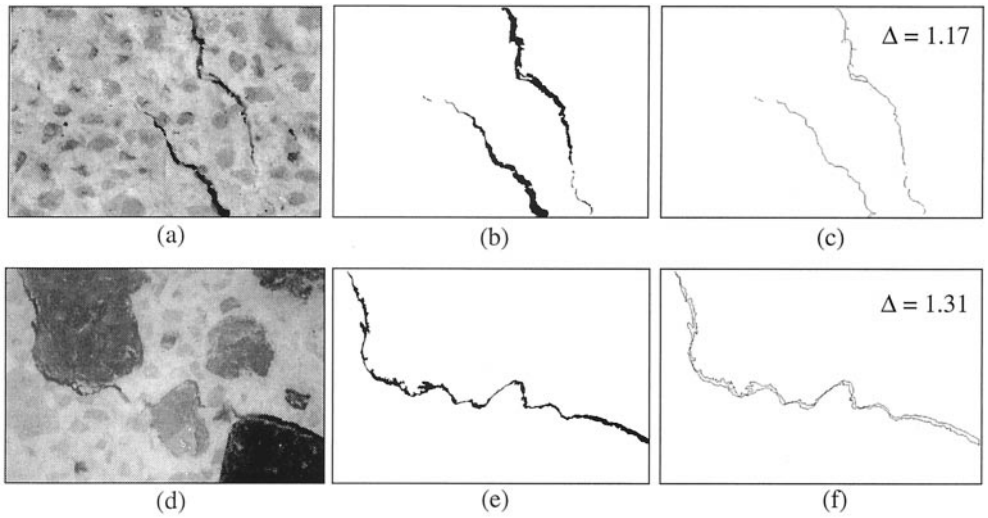

FIG. 5.
Image processing on a ConPS crack bridging pattern (*a*, *b*, *c*) and on a Con2 single crack (*d*, *e*, *f*).

dimensions of the cracks, it is also possible to use each disconnected (original) image for retrieving detailed information of the mosaic. It will be shown that the mosaics properly describe the transition from the fractal disordered patterns detected at the highest magnifications to the euclidean domains that are observed when the scale of observation decreases.

In order to extract the topological information about the damage patterns, filtering of the images is necessary. Starting from complex gray level images (Figs. 5a, d), pixels belonging to the cracks have to be selected and isolated. Due to the dark colour of the cracks, thresholding has proven to be the most effective routine. However, this does not turn into a straightforward procedure because discrimination between cracks and dark particles is extremely difficult, as can be realized by considering the relatively homogeneous histogram of gray values. Prior to thresholding, enhancing the contrast in the image is a useful tool for distinguishing more clearly the crack boundaries from their surrounding. This was obtained by eliminating a sufficient number of gray levels to yield a discontinuous histogram. Next, the filtered images were thresholded and arrays of black and white pixels were generated (Figs. 5b, e). Because a unique gray level threshold could not be adopted for a single image, selective filtering was applied to different parts of the image, choosing for each zone the most appropriate threshold value. This gray level ranged between 80 and 135.

After thresholding, binary thinning of the cracks was applied in two different ways. When the complex network of diffused microcracking had to be analysed, an algorithm was used that yielded skeletonized cracks by averaging black pixels through the width (Fig. 5c). A serious drawback was the loss of many details from the crack boundaries, resulting in smoother skeletonized patterns, not properly representing the complexity of the energy dissipation that takes place at the crack lips. Therefore, when the lips of a main crack had to be examined, a second algorithm was developed to shrink the cracks by outlining their boundaries. This approach proved very successful in the case of self-affine propagating cracks, because in this way it was possible to highlight the crack lip's irregularities orthog-

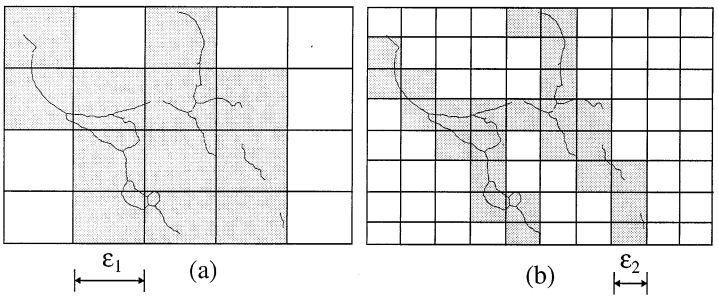

$$\Delta = \lim_{\varepsilon_i \to 0} \left(\frac{\log N(\varepsilon_i)}{\log (1/\varepsilon_i)} \right)$$

FIG. 6.
The box-counting method applied to a Con2 crack pattern. The fractal dimension is equal to 1.127.

onal to the advancement direction (Fig. 5f). On the other hand, when complex self-similar networks were digitized, the first algorithm prevailed.

Once the damage patterns have been filtered, either in the case of self-similar networks or in the case of self-affine crack lips, their fractal dimension is computed by means of the box-counting method (Fig. 6). This method represents the most general deterministic algorithm for the case of natural fractals (4). The filtered image is covered by means of rectangular grids of progressively decreasing linear size. The fractal dimension is obtained by computing the logarithmic density of the measure of these coverings, as their linear size decreases. The omothetical and progressive shrinking of the covering grids implies isotropic scaling of the covering shape. This could be in contrast with the eventually anisotropic (self-affine) properties of the fractal domain. Therefore, direction-dependent rescaling of the grid size was performed in the case of self-affine cracks. On the contrary, in the case of self-similar damage, it seemed more convenient to use isotropic square coverings of the image. A minimum box size equal to one pixel (which means roughly 1.4 mm^2 and 3.7 mm^2, respectively, for the highest and the lowest magnification factor) was adopted.

Fractal Analysis of Digitized Crack Patterns

The optical detection of the damage near the crack tip permits highlighting of some morphological differences in the fracture behaviour of the different concretes, which correspond to the previously described mechanical differences. The interface between large aggregates and matrix represents the weakest link of the four composites. Non-integer Hausdorff dimensions of the damage patterns have been determined in all four mixtures (see Table 1). This confirms that, at the proper scales, the phenomenon of fracture in heterogeneous media possesses a well-defined fractal character.

In the case of the ConPS, the propagation of the cracks is almost totally controlled by the bond strength. The relatively smooth shape of the aggregates provides a weak obstacle to crack propagation (Fig. 7a). Brittle local debonding, due to the low toughness/strength ratio, causes micro-instabilities during the loading process. This was observed also in a single aggregate experiment with a stiff granite aggregate (5). If the fractal dimension of the interface crack in Figure 7c is computed, one obtains $\delta = 1.08$, which represents a rather low value. On the other hand, micro-bridging and multiple cracking come into play in the matrix,

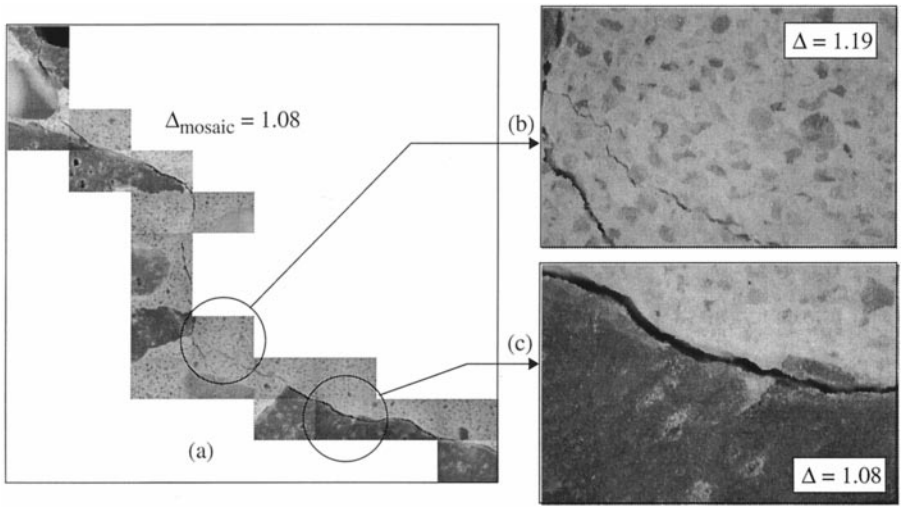

FIG. 7.
Damage in ConPS: complete crack path (*a*), bridging in the matrix (*b*) and brittle debonding (*c*).

(Fig. 7b). A rather high fractal dimension ($\delta = 1.19$) is found in this case. This accounts for a more stable propagation of the cracks in the matrix with respect to the interface zones. A more brittle structural behaviour is globally provided by ConPS, when compared to the normal or Lytag mixtures. Image analysis on the crack patterns detected on Con16 shows similarities with ConPS, but larger fractal dimensions are obtained in this case. Interface cracks appear rougher and matrix damage is more diffuse. The complete paths represented by the mosaics are also more complex (Fig. 4b), even if interfaces still play the role of main attractors for propagation. This indicates a more ductile mechanical behaviour.

When the aggregate strength becomes comparable to the strength of the matrix, interface properties play a less pronounced role. The high porosity of the Lytag aggregate causes a dense and strong interface. A stronger bond between the matrix and the particle results in a more homogeneous damage propagation. On the other hand, the intrinsic weakness of the Lytag particles leads to a reduced crack-arresting capacity in the lightweight concrete.

The crack path mosaic in Figure 8a clearly shows how macrocracks can propagate also through the aggregates. In the Lytag concrete, cracks have an almost equal probability of either following the (relatively strong) interfaces or going through the particles. This is because the crack resistance is approximately the same in both cases. Therefore, local instabilities (snap-backs) are almost absent compared to ConPS. Through-particle cracks (Fig. 8c) behave in a stable manner due to the microscopic heterogeneity of the Lytag particles. The rather high values of δ recall the microscopic complexity revealed in the single aggregate experiments on sandstone (10). This may be the reason for the relevant structural ductility found for this mixture, which is not obvious if related to its low toughness and strength. Moreover, a reduced sensitivity to thermic and drying-shrinkage cracking is present, due to the similar elastic modulus possessed by the matrix and the Lytag aggregates.

In the case of Lytag and Con2, peculiar aspects of a more homogeneous behaviour (at the specimen level) are in evidence, such as cracks occurring through the particles in the Lytag

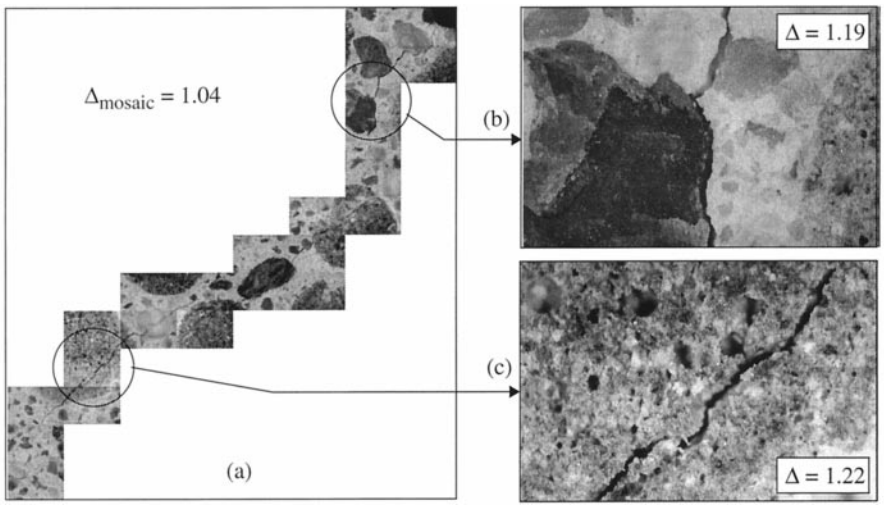

FIG. 8.
Damage in Lytag: complete crack path (*a*), matrix cracking (*b*) and through-particle crack (*c*).

and the relative smoothness of the fracture patterns in the Con2. On the other hand, microscopic bridging (1) is activated at the scale of sand grains in the Con2 (Fig. 4a), just as rough fractal cracks grow through the Lytag particles (Fig. 8c). This means that disorder is equally present in these two materials, but at a lower level of observation as compared to Con16 and ConPS. Therefore, Con2 and Lytag can be characterized as having a smaller characteristic material length. This explains, as stated before, the lower scatter that was found in the measurement of their mechanical properties.

Conclusions

In this paper it was shown that the stiffness, strength, and density of the aggregates strongly affect the global behaviour of the concrete mixture. The failure mechanism is affected substantially by the strength ratios of the three phases in the material, i.e., matrix, aggregate, and interface bond between matrix and aggregate. The optical analysis strongly suggests that the phenomenon of fracture is highly complex and that different fracture mechanisms occur at different scales. The variable role of the microstructural disorder on the mechanical properties of materials can be captured by the fractal analysis. Fractality implies self-organized dissipation, and this increases ductility and may even promote crack-arrest. Results are summarized in Table 1. It should be noted that, as the resolution of the image decreases, the fractal dimension decreases as well. This is clear in Figures 7 and 8, where the fractal dimension of the mosaic pattern is much lower than the fractal dimension of the single high-resolution images. This implies a transition from fractal microscopic damage towards homogeneous patterns at larger scales (geometrical multifractality). The progressive homogenization of the microstructural fluctuations provides, at the structural scale, the progressive vanishing of the size effects for increasing structural size (4).

Lytag and Con2 show lower scatter of the measured mechanical properties, as compared to Con16 and ConPS. This can be explained by a lower degree of disorder that is due to the

relative homogeneity between matrix and particles in the case of Lytag, and to the finer microstructure of Con2. In any case, if the mean values of the fractal dimension δ of the concretes are compared (Table 1), it can be stated that homogenization of the disordered microstructure is observed earlier for the case of lightweight concrete and mortar. Thus, less sensitivity to size-effects is present in these two composites. These results suggest that the minimum representative size of the fracture specimens should be related to the microstructural characteristics of the considered material.

Higher fractal dimensions do not necessarily imply higher toughness in a material, because disordered fracture patterns may be the consequences of both weak (pores, bonds) and strong (aggregates, inclusions) heterogeneities. Another interesting consequence of our results is that including weaker elements in the composite can increase ductility. These can either be the aggregates, the bond zone, or a very weak matrix. In the splitting tests, no clear correlation was found between the computed fractal dimensions and the measured fracture energy. Instead, fractality permits us to explain the stable crack growth occurring in the first stages of the tests, physically related to the smoothing of the stress-singularity (6).

References

1. S. Mindess, Materials Science of Concrete I, J.P. Skalny (ed.), p. 163, Am. Ceram. Soc., Westerville, OH, 1989.
2. J.G.M. van Mier, Cem. Concr. Res. 21, 1 (1991).
3. A. Hillerborg, M. Modéer, and P.E. Petersson, Cem. Concr. Res. 6, 773 (1976).
4. A. Carpinteri and B. Chiaia, Mater. Struct. 29, 259 (1996).
5. A. Vervuurt, Interface Fracture in Concrete. Delft, Netherlands: Delft Univ. of Tech.; Ph.D. Thesis. 1997.
6. A. Carpinteri and B. Chiaia, Int. J. Fract. 76, 327 (1995).
7. E. Schlangen and J.G.M. van Mier, Cem. Concr. Compos. 14, 105 (1992).
8. J.G.M. van Mier, B. Chiaia, and A. Vervuurt, Comp. Meth. Appl. Mech. Eng. 142, 189 (1997).
9. H.N. Linsbauer and E.K. Tschegg, Zement und Beton 31, 38 (1986).
10. A. Vervuurt, B. Chiaia, and J.G.M. van Mier, Heron 40, 285 (1995).